energies

MDPI

Article

P-Y Curve Correction of Shallow Seabed Formation Containing Hydrate

Haoyu Diao [1,*], Honghai Fan [1], Rongyi Ji [1], Bangchen Wu [1], Yuguang Ye [1], Yuhan Liu [2], Fei Zhou [1], Yixiang Yang [1] and Zhi Yan [1]

[1] College of Petroleum Engineering, China University of Petroleum-Beijing, 18, Fuxue Road, Changping District, Beijing 102249, China
[2] CNPC Engineering Technology R&D Company Limited, Beijing 102206, China
* Correspondence: 2018312010@student.cup.edu.cn or diaohaoyudhy@163.com; Tel.: +86-155-1063-9178

Abstract: With the continuous growth in global energy demand, the exploration and development of hydrates has been the focus of increasing attention, and the accurate evaluation of the mechanical properties of hydrate layers has become particularly important. In this study, using a self-developed hydrate sample preparation device and hydrate triaxial seepage test platform, triaxial shear tests were carried out using the in situ synthesis method for hydrate sediment in the laboratory, and the stress–strain curves of hydrate sediment with different levels of saturation were obtained. By analyzing the stress–strain curve, the mechanical parameters of hydrate sediment were calculated and simulated using ABAQUS (2021, Dassault systemes, Vélizy Villacoublay France) finite element software. Several p-y curves were calculated and compared with the simulation results, and the p-y curve correction method of the hydrate layer in a shallow seabed was obtained. It was found that the strength of the hydrate sediment increased with an increase in saturation. At the same time, an increase in confining pressure and a decrease in temperature also increased the strength of hydrate deposits. Through comparison with the existing API (American Petroleum Institute) standard p-y curve, it was found that its strength is low because the existence of the hydrate improves the formation strength.

Keywords: methane hydrate; triaxial shear test; mechanical property; numerical simulation; p-y curve

Citation: Diao, H.; Fan, H.; Ji, R.; Wu, B.; Ye, Y.; Liu, Y.; Zhou, F.; Yang, Y.; Yan, Z. P-Y Curve Correction of Shallow Seabed Formation Containing Hydrate. *Energies* **2023**, *16*, 3274. https://doi.org/10.3390/en16073274

Academic Editor: Devinder Mahajan

Received: 13 March 2023
Revised: 29 March 2023
Accepted: 30 March 2023
Published: 6 April 2023

1. Introduction

Gas hydrate is an ice-like crystalline solid composed of water and natural gas which is stable under high-pressure and low-temperature conditions, and naturally occurs in permafrost and offshore areas [1–3], of which marine gas hydrate reserves account for more than 90% of the total reserves [4,5]. With the intensification of global warming and the frequent occurrence of extreme weather events, especially the carbon dioxide emission value and the need for carbon neutrality, global energy consumption is facing a huge adjustment. Gas hydrate has become one of the most promising alternative energy sources in the development of global economic plans due to its low-carbon properties [6,7]. The reserves of natural gas hydrates in the world are approximately 1×10^{17} m^3 and 3×10^{20} m^3 [8,9]. The occurrence area of marine gas hydrate has the characteristics of shallow buried depth, weak cementation, most of which have no tight caprock, and well-developed source-reservoir caprock [10–12]. Moreover, due to the special environmental conditions such as the low temperature and the high pressure of the hydrate layer, its physical properties are different from those of traditional seabed sediments, representing huge challenges in exploration and development, and also bringing great challenges and security risks to seabed engineering operations such as offshore drilling and completion. With the continuous growth in global energy demand, the exploration and development of hydrates are receiving more and more attention.

There have been some studies on the mechanical properties of hydrate sediments and shallow seafloor formations. Li et al. [13] compared and analyzed the preparation methods of hydrate samples, and found that although the related parameters of the mixed sample preparation method are easy to control and the hydrates are more uniformly distributed in the samples, the loss of hydrates can easily occur, which is more likely than that with situ generation. The experimental precision of the method is poor. Luo et al. [14] conducted triaxial shear tests on hydrate sediment samples from the Pearl River Mouth Basin in the South China Sea and hydrate samples synthesized in the laboratory, and found that their stress–strain characteristics were the same under the same test conditions. Miyazaki et al. [15] conducted triaxial compression tests on hydrate deposits with different particle sizes of quartz sand and Toyoura sand as the framework. The type of sand influences the stiffness of hydrate deposits, but has little effect on the strength. Masayuki et al. [16] conducted triaxial compression tests on hydrate deposits with different fine particle contents and densities, and found that the increase in fine particle content would reduce the porosity of hydrate deposits, leading to an increase in shear strength and stiffness. According to the characteristics of argillaceous silt hydrate, Li et al. [17] proposed a method of evaluating the hydrate content using the average mass abundance instead of saturation, and carried out a triaxial mechanical study on argillaceous silt THF (tetrahydrofuran) hydrate. Performing parametric testing, Zhu et al. [18] conducted triaxial compression experiments on methane and carbon dioxide hydrate deposits, and compared the mechanical properties of the two hydrate deposits. Li [19] studied the lateral dynamic response of pile foundation in liquefied soil layers, and proposed the p-y curve correction method and correction model. Qi [20] studied the p-y curve of pile–soil interactions in the process of saturated sand liquefaction and proposed a three-stage and hyperbolic form of a weakening p-y curve correction method. However, there are no studies on the p-y curve of shallow hydrate-bearing formations in the existing literature.

The aim of this study was to use the self-developed hydrate preparation device and triaxial-seepage test device to obtain stress–strain curves through triaxial shear tests in order to study the mechanical properties of hydrates and to analyze the effects of saturation, temperature, and confining pressure on hydrates. To determine the influence of sediment strength, the mechanical parameters related to hydrate deposits were calculated through the stress–strain curve and the self-compiled MATLAB program (version R2022a, MathWorks, Natick, MA, USA). Numerical simulations under actual working conditions were carried out using ABAQUS, and the p-y curves of multiple hydrate layers were calculated. Based on the p-y curve of API specification, a p-y curve correction method for the hydrate layer is proposed.

2. Materials and Methods

2.1. Hydrate Sample Preparation Device and Triaxial-Seepage Test Platform

By designing and processing the hydrate sample preparation device and the hydrate triaxial-seepage test platform, we tested the mechanical properties of natural gas hydrate by the in situ synthesis of hydrate samples under laboratory conditions. Additionally, we simulated the seepage process of gas in the hydrate layer under real stress conditions. This platform could also be used to study the triaxial mechanical properties and seepage characteristics of other rock cores.

2.1.1. Main Functions of the Test Device

(1) Processing and preparation of hydrate samples

The real temperature and pressure conditions of hydrate formation were simulated, and the in situ synthesis of hydrate samples was completed.

(2) Uniaxial compression test

Under low-temperature conditions, during the compression process of axial pressure applied in one direction, the relationship between the stress and the deformation (displacement) of the hydrate sample (or conventional core sample) was measured.

(3) Triaxial compression test

Under low-temperature conditions, during the process of applying confining pressure and axial pressure compression, the relationship between the stress and deformation of hydrate samples (or conventional core samples) was measured.

(4) Permeability measurement test under real formation pressure conditions

Under constant-temperature conditions, the permeability of hydrate samples (or conventional core samples) was measured. At the same time, the pore pressure in the sample could also be controlled.

(5) Permeability measurement test under real formation pressure conditions

Under the condition of constant temperature, the permeability of the hydrate sample (or conventional core sample) was measured during the process of applying confining pressure and axial pressure compression. Net confining pressure could also be controlled during triaxial compression.

2.1.2. Key Points and Methods of Test Design

(1) Key points of test design

In the process of configuring hydrate samples, it should be ensured that the physical properties of the samples are as similar as possible to the real hydrate reservoirs.

During the preparation of hydrate samples, we aimed to minimize the influence of temperature increases on hydrate formation caused by the work done by compressing the volume.

The stability of hydrates is greatly affected by temperature and pressure. During the preparation and transfer of hydrate samples, the temperature and pressure conditions should be controlled as much as possible to reduce the impact of hydrate decomposition on test results.

During the test process, due to the work done by the compressed volume, the temperature and pressure conditions will change; thus, the test process should be kept at a constant temperature to reduce the decomposition of hydrates and maintain the stability of the sample.

(2) Hydrate sample preparation device

The main body of the hydrate sample preparation device is a hydrate sample preparation kettle which can simulate the real temperature and pressure conditions of a hydrate layer to prepare weakly cemented hydrate samples and cemented samples. The main body of the preparation kettle is cylindrical, and the cylinder wall encloses the interior of the kettle into a cylindrical space. The upper part is sealed by the steel shaft of the pressure control system, and the lower part has a gas channel for the introduction of reaction gas. In order to ensure the gas sealing effect, sealing rings are added on the upper and lower parts.

The pressure control system of the sample preparation device consists of two parts: the air pressure control system and the axial pressure control system. The air pressure control system consists of a vacuum pump and a gas cylinder. Before the reaction, the preparation device is evacuated by the vacuum pump to avoid the interference of other gases, and then the test gas is introduced through the gas cylinder to control the gas pressure in the device, which can be used for hydrates. This provides the necessary pressure conditions for the formation of hydrates; the axial pressure control system controls the pressure through the hydraulic pump, which can provide the necessary pressure conditions for the compaction of hydrate samples.

(3) Hydrate triaxial-seepage test platform

Figure 1a is a schematic diagram of a hydrate three-axis-seepage platform which mainly includes a reactor, an axial pressure-loading system, a confining pressure-loading system, a temperature control system, an injection system, an output system, a gas cylinder, a data acquisition and control system, a support, and a flow pump. All systems except for the support and gas cylinders were connected to the computer for control; the axial pressure-loading system was loaded by hydraulic control pressure; the support mode of the support was a column type; the circulating fluid medium of the temperature control

system was antifreeze; and the fluid media of the injection system and the output system were all gases.

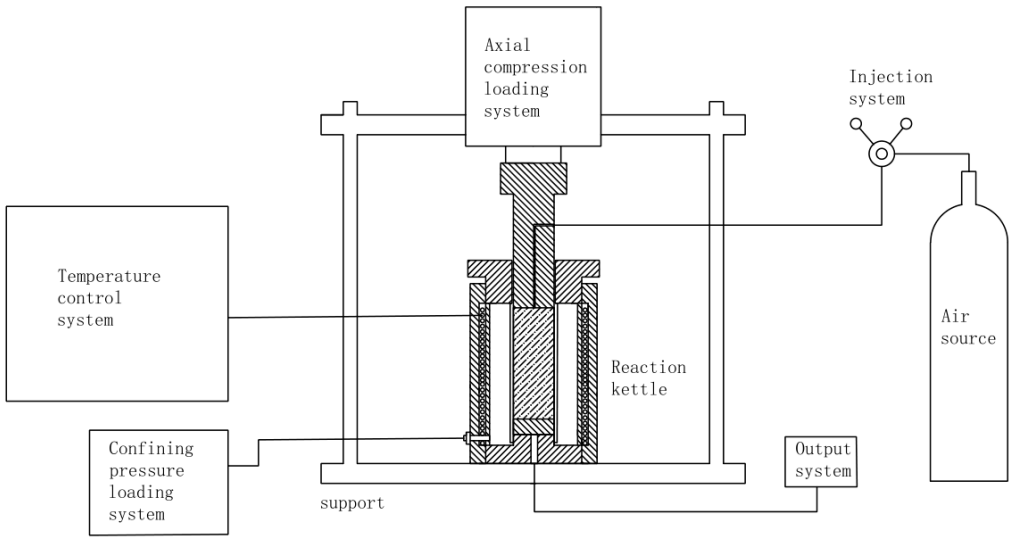

(**a**)

(**b**)

Figure 1. Hydrate triaxial-seepage test platform. (**a**) Schematic diagram of the hydrate triaxial-seepage test platform. (**b**) Physical picture of the hydrate triaxial-seepage test platform.

2.2. Physical Property Evaluation and Preparation Method of Natural Gas Hydrate Samples

2.2.1. Preparation Method of Natural Gas Hydrate Samples

Marine gas hydrate reservoirs can be divided into two types according to lithology: consolidated diagenetic and weakly cemented non-diagenetic. The consolidated diagenetic hydrate layer is supported by the formation skeleton, and the reservoir does not deform or deforms slightly after the hydrate is decomposed. The formation framework of non-

diagenetic hydrates is poorly cemented and cannot provide complete support; therefore, the hydrates must undertake part of the supporting role of the reservoir, and the reservoir will collapse or deform after the hydrates decompose. The samples used in the test in this paper were diagenetic (cemented), with good cementation strength. The diagenetic sample (sandy core) was obtained by pressing 120–180 μm (80–100 mesh) quartz sand.

Heat is generated during the formation of hydrates. In theory, it can be judged whether hydrates are formed through temperature changes. However, due to the need to circulate antifreeze through the temperature control system to maintain a constant low temperature during the sample preparation process, the heat generated during the hydrate formation process will be quickly taken out of the test device; thus, the temperature change in the reactor cannot be used as the main reason for hydrate formation. Therefore, we chose to judge whether there was natural gas hydrate formation according to the drop in reactor pressure.

Whether the hydrate was completely formed had a considerable influence on the physical parameters of the sample; thus, it was very important to ensure complete hydrate formation in the preparation kettle at the end of the sample preparation to guarantee the success of the test. When the pressure in the preparation kettle was stable above the phase equilibrium pressure for a long time and did not decrease after pressurization, the sample preparation was completed.

2.2.2. Physical Property Evaluation Methods of Hydrate Samples

The natural gas hydrates found in the South China Sea are mainly Type I methane hydrates. Moreover, what was prepared in this experiment was also a type I methane hydrate; therefore, mainly type I methane hydrate was studied here, and the relevant parameters were selected from type I methane hydrate parameters.

The unit cell of type I methane hydrate is composed of 46 water molecules, including two small cavities and six large cavities, which can accommodate small molecular gases such as CH_4, N_2, CO_2, H_2S, etc.; their chemical formula is $6X{\cdot}2Y{\cdot}46H_2O$ [21].

(1) Hydration number of the hydrate

The P-R equation (real gas state equation) can be used to calculate the compressibility factor of methane:

$$\begin{cases} P = \frac{RT}{V_m - b} - \frac{a(T)}{V_m(V_m+b)+b(V_m-b)} \\ a(T) = 0.45724\frac{R^2T_c^2}{P_c}\left[1 + m\left(1 - \frac{T}{T_c}\right)^{\frac{1}{2}}\right]^2 \\ b = 0.07780\frac{RT_c}{P_c} \\ m = 0.37464 + 1.54226\omega - 0.26992\omega^2 \end{cases} \quad (1)$$

The form of the P-R equation expressed by the compression factor, z, is as follows:

$$\begin{cases} z^3 - (1-B)z^2 + (A - 2B - 3B^2)z - (AB - B^2 - B^3) = 0 \\ A = \frac{aP}{R^2T^2} \\ B = \frac{bP}{RT} \end{cases} \quad (2)$$

where P is the pressure, MPa; T is the temperature, K; V_m is the molar volume of methane gas, L/mol; R is the universal gas constant; 8.314 J/(mol·K); $a(T)$, b, m, A, and B are the parameters of the state equation; T_c is the critical temperature of methane, 190.67 K; P_c is the critical pressure of methane, 4.6408 MPa; and ω is the eccentricity factor of methane, 0.0115.

In the hydrate cage structure, the guest molecule reacts with water, and the formula for forming the hydrate is as follows:

$$G(g) + N_hH_2O(l) \rightleftarrows G{\cdot}N_hH_2O(s) \quad (3)$$

where $G(g)$ is the guest molecule and N_h is the hydration number of the hydrate.

The hydrate indices in the Pearl River Mouth Basin and the Shenhu Sea Area are 5.90 and 5.99, respectively, both of which are higher than the theoretical value of 5.75, but

lower than 6.06 for the synthesis of methane hydrate. The reason is that the hydrate cavity occupancy rate is different [22]. In this study, the following method was used to calculate the hydration number of methane hydrate [23]:

$$\begin{cases} N_{\mathrm{h}} = \frac{46}{6\theta_{\mathrm{l}}+2\theta_{\mathrm{s}}} \\ \theta_i = \frac{C_i f}{1+C_i f} \\ \ln\frac{f}{P} = Z - 1 - \ln\frac{P(V-b)}{RT} - \frac{\alpha(T)}{2\sqrt{2}bRT}\ln\frac{V+\left(\sqrt{2}+1\right)b}{V-\left(\sqrt{2}-1\right)b} \end{cases} \tag{4}$$

where N_{h} is the hydration number of the hydrate; θ_{l} and θ_{s} are the occupancy ratios of the large cavity and the small cavity of the hydrate, %; and f and C_i are the gas fugacity and Langmuir constant [24].

$$C_i = \frac{A_i}{T} e^{\left(\frac{B_i}{T}+\frac{D_i}{T^2}\right)} \tag{5}$$

where A_i and B_i are the calculation coefficients of the Langmuir constant, whose values are shown in Table 1.

Table 1. Calculation parameters of the Langmuir constant of methane.

Small Cavity			Large Cavity		
A_i(K/MPa)	B_i(K)	$D_i\left(\mathrm{K}^2\right)$	A_i(K/MPa)	B_i(K)	$D_i\left(\mathrm{K}^2\right)$
0.04397	2491.66	0.04483	0.17218	2485.24	0.03437

(2) Phase equilibrium condition

The statistical thermodynamic method was used to calculate the phase equilibrium conditions for hydrate formation in this study.

The process of gas hydrate formation is a process in which gas, liquid, and solid phases coexist; thus, the thermodynamic model of gas hydrate needs to consider the hydrate phase and water-rich phase models.

When the gas hydrate phase is in equilibrium [25,26]:

$$\begin{cases} \Delta\mu_{\mathrm{H}} = \mu_\beta - \mu_{\mathrm{H}} = RT\sum\limits_{i=1}^{2}\nu_i \ln\left(1 - \sum\limits_{j=1}^{N_{\mathrm{c}}}\theta_{ij}\right) \\ \theta_{ij} = \frac{C_{ij}f_j}{1+\sum\limits_{j=1}^{N_{\mathrm{c}}}C_{ij}f_j} \end{cases} \tag{6}$$

where μ_β and μ_{H} are the chemical potentials of water in the empty hydrate (β phase) and hydrate phase, cal/mol; ν_i is the number of i-type pores in the unit water molecule in the hydrate phase; θ_{ij} is the occupancy of guest gas molecule j in i-type pores; N_{c} is the number of components that can generate natural gas hydrate in the miscible phase; C_{ij} is the Langmuir constant of the guest molecule j in the i-type pores; and f_j is the fugacity of component j in the equilibrium in each phase.

When gas hydrates and non-gas hydrates are in equilibrium:

$$\mu_{\mathrm{w}} + RT\sum_{i=1}^{2}\nu_i \ln\left(1 - \sum_{j=1}^{N_{\mathrm{c}}}\theta_{ij}\right) = \mu_{\mathrm{w}}^0 + RT\ln\left(\frac{f_{\mathrm{w}}}{f_{\mathrm{w}}^0}\right) \tag{7}$$

where μ_{w} and f_{w} are the chemical potential and fugacity of water in the water-rich phase, respectively; μ_{w}^0 and f_{w}^0 are the chemical potential and fugacity of pure water in the reference states T and P, respectively.

The chemical potential difference of water can be expressed as:

$$\frac{\mu_{\mathrm{w}}\mu_{\mathrm{w}}^{0}}{RT} = \frac{\Delta\mu_0}{RT_0} - \int_{T_0}^{T} \frac{\Delta H_0 + \Delta \mathrm{C_p}(T - T_0)}{RT^2}\mathrm{d}T + \int_{P_0}^{P} \frac{\Delta V}{RT}\mathrm{d}P \tag{8}$$

Simultaneously solving Equations (7) and (8) can obtain the hydrate phase equilibrium condition:

$$\frac{\Delta\mu_0}{RT_0} - \int_{T_0}^{T} \frac{\Delta H_0 + \Delta C_p(T - T_0)}{RT^2}\mathrm{d}T + \int_{p_0}^{p} \frac{\Delta V}{RT}\mathrm{d}P = \ln\left(\frac{f_{\mathrm{w}}}{f_w^0}\right) - \sum_{i=1}^{2} \nu_i \ln\left(1 - \sum_{j=1}^{N_c} \theta_{ij}\right) \tag{9}$$

In the formula, $\Delta\mu_0$ is the chemical potential difference between the empty gas hydrate lattice and pure water in the standard state; T_0 is the standard temperature, 273.15 K; P_0 is the standard pressure, 0.1 MPa; ΔH_0 is the specific enthalpy difference, specific tolerance difference, and specific heat tolerance difference between the air–gas hydrate lattice and pure water; and $\ln\left(f_{\mathrm{w}}/f_{\mathrm{w}}^0\right) = \ln x_{\mathrm{w}}$, x_{w} is the mole fraction of water in the water-rich phase.

(3) Density of hydrate

In this study, the analytical gas method was used to calculate the amount of methane consumption. In order to avoid the influence of air and hydrate decomposition on the collected methane volume, the hydrate sample should be decomposed after the sample preparation is completed. The solubility of methane in water is extremely small, and the methane gas dissolved in water is negligible; therefore, the drainage method was used to collect methane gas.

$$V_{\mathrm{dr}}^{\mathrm{m}} = V_{\mathrm{dr}}^{\mathrm{w}} = \frac{m_{\mathrm{dr}}}{\rho_{\mathrm{w}}} \tag{10}$$

where $V_{\mathrm{dr}}^{\mathrm{m}}$ and $V_{\mathrm{dr}}^{\mathrm{w}}$ are the volumes of methane and water collected by the drainage method, respectively, cm^3; m_{dr} is the mass of water collected by the drainage method, g; and ρ_{w} is the density of water at laboratory temperature, $\mathrm{g/cm}^3$.

The preparation kettle was in a vacuum state before the gas was added during the preparation of the hydrate sample; therefore, the gas in the pores could not be completely discharged after the hydrate was decomposed, and the residual gas mass in the sample pores should also be considered when calculating the mass of methane consumed. Compared with the formation of hydrate, the aeration of gas pressurization is a rapid process; thus, the amount of methane consumed by hydrate formation during aeration is negligible. The amount of methane consumed to generate hydrates can be calculated by the following formula:

$$\begin{cases} n_{\mathrm{m}} = n_{\mathrm{dr}} - n_{\phi}^{\mathrm{h}} + n_{\phi} \\ n_{\mathrm{dr}} = \frac{V_{\mathrm{dr}}^{\mathrm{m}}}{V_{\mathrm{m}}^{\mathrm{T}}} = \frac{V_{\mathrm{dr}}^{\mathrm{m}}}{\frac{V_{\mathrm{m}}}{T_{\mathrm{m}}}T_{\mathrm{dr}}} \\ n_{\phi}^{\mathrm{h}} = \frac{P_{\mathrm{h}}\left(V_{\phi}^{\mathrm{h}} - V_{\mathrm{l}} - V_{\mathrm{h}}\right)}{zRT_{\mathrm{h}}} \\ n_{\phi} = \frac{P\left(V_{\phi} - V_{\mathrm{l}}\right)}{zRT} \end{cases} \tag{11}$$

where n_{m} is the amount of substances that consume methane to form hydrates, mol; n_{dr} is the amount of methane collected by the drainage method, mol; n_{ϕ} and n_{ϕ}^{h} are the amount of methane in the pores before and after hydrate formation, respectively, mol; $V_{\mathrm{dr}}^{\mathrm{m}}$ is the volume of methane collected by the drainage method, cm^3; $V_{\mathrm{m}}^{\mathrm{T}}$ and V_{m} are the molar volume of gas under laboratory temperature and pressure and STP, $\mathrm{cm}^3/\mathrm{mol}$; T_{dr} and T_{m} are the laboratory temperature and standard temperature, respectively, K; P_{h} and P are the pressure in the preparation tank before and after hydrate decomposition, respectively, MPa; V_{ϕ}^{h} and V_{ϕ} are the pore volume of the sample before and after hydrate decomposition, respectively; V_{l} is the volume of SDS (sodium dodecyl sulfate) solution consumed by the reaction, cm^3; V_{h} is the volume of hydrate formed by the reaction; T_{h} and

T are the temperature in the preparation kettle before and after hydrate decomposition, K, respectively.

The volume of hydrate formed in the test can be calculated by the following formula:

$$V_{\mathrm{h}} = \frac{n_{\mathrm{m}}}{46} N_{\mathrm{h}} \mu_{\omega}^{\mathrm{h}} = \frac{n_{\mathrm{dr}} - n_{\phi}^{\mathrm{h}} + n_{\phi}}{46} N_{\mathrm{h}} \mu_{\omega}^{\mathrm{h}} \tag{12}$$

where V_{h} is the volume of hydrate formed, cm^3; n_{m} is the amount of substances that consume methane to form hydrates, mol; n_{dr} is the amount of methane collected by the drainage method, mol; n_{ϕ} and n_{ϕ}^{h} are the amount of methane in the pores before and after hydrate formation, respectively, mol; and N_{h} is the hydration number of the hydrate; $\mu_{\omega}^{\mathrm{h}}$ is the lattice molar volume of hydrate, $\mathrm{cm}^3/\mathrm{mol}$, which can be calculated using Equation (13) [27,28].

$$\begin{cases} \mu_{\omega}^{\mathrm{h}} = [\beta(T)]^3 \times 10^{-30} \times N_{\mathrm{A}} \times 10^6 \\ \beta(T) = 11.835 - 1.12 \times 10^{-4} T + 2.47 \times 10^{-6} T^2 \end{cases} \tag{13}$$

where $\mu_{\omega}^{\mathrm{h}}$ is the lattice molar volume of the hydrate, $\mathrm{cm}^3/\mathrm{mol}$; $\beta(T)$ is the hydrate lattice parameter, 0.1 nm; and N_{A} is Avogadro's constant, $6.02 \times 10^{23} \mathrm{mol}^{-1}$.

The pore volume of hydrate deposits (before hydrate formation) can be calculated using the following formula:

$$V_{\phi} = V_{\mathrm{samp}} - V_{\mathrm{sand}} = \frac{\pi}{4} d_{\mathrm{samp}}^2 h_{\mathrm{samp}} - \frac{m_{\mathrm{sand}}}{\rho_{\mathrm{sand}}} \tag{14}$$

where V_{ϕ} is the pore volume of the hydrate deposit, cm^3; V_{samp} is the volume of the hydrate sample, cm^3; V_{sand} is the volume of quartz sand, cm^3; d_{samp} and h_{samp} are the diameter and height of the hydrate sample, respectively, cm; m_{sand} is the quality of quartz sand, g; and ρ_{sand} is the density of quartz sand, g/cm^3.

The pore volume of hydrate deposits (before hydrate decomposition) can be calculated using the following formula:

$$\begin{cases} V_{\phi}^{\mathrm{h}} = V_{\mathrm{samp}} - V_{\mathrm{sand}} - V_{\mathrm{h}} \\ V_{\mathrm{samp}} = \frac{\pi}{4} d_{\mathrm{samp}}^2 h_{\mathrm{samp}} \\ V_{\mathrm{sand}} = \frac{m_{\mathrm{sand}}}{\rho_{\mathrm{sand}}} \end{cases} \tag{15}$$

where V_{ϕ}^{h} is the pore volume of the hydrate sample, cm^3; V_{samp} is the volume of the hydrate sample, cm^3; V_{sand} is the volume of quartz sand, cm^3; V_{h} is the volume of hydrate formed, cm^3; d_{samp} and h_{samp} are the diameter and height of the hydrate sample, cm, respectively; m_{sand} is the quality of quartz sand, g; and ρ_{sand} is the density of quartz sand, g/cm^3.

In the experiment, 0.3 g/L SDS solution was used instead of deionized water to promote the formation of hydrate, but the solubility of SDS is very low; therefore, the influence of SDS on the molar volume of water could be ignored. The volume of SDS solution consumed by the hydrate reaction can be calculated using Equation (16):

$$V_{\mathrm{w}} = N_{\mathrm{h}} \times n_{\mathrm{m}} \times \mu_{\omega}^{\mathrm{l}} \tag{16}$$

where V_{w} is the volume of water consumed by the reaction, cm^3; n_{m} is the amount of methane consumed by the formation of hydrate, mol; and $\mu_{\omega}^{\mathrm{l}}$ is the molar volume of the SDS solution, $\mathrm{cm}^3/\mathrm{mol}$, which can be calculated using Equation (17) [29]:

$$\begin{aligned} \mu_{\omega}^{\mathrm{l}} \quad &= 18.015 \times \left[1 - \left(1.001 \times 10^{-2}\right) + \left(1.33391 \times 10^{-4}\right) \times (1.8 \times T + 32)^2 \right. \\ &\quad \left. + \left(5.50654 \times 10^{-7}\right) \times (1.8 \times T + 32)\right] \times 10^3 \end{aligned} \tag{17}$$

where $\mu_{\omega}^{\mathrm{l}}$ is the molar volume of SDS solution, $\mathrm{cm}^3/\mathrm{mol}$.

The prepared hydrate density can be calculated using the following formula:

$$\rho_{\mathrm{h}} = \frac{(6\theta_{\mathrm{l}} + 2\theta_{\mathrm{s}})M_{\mathrm{m}} + 46M_{\mathrm{w}}}{\mu_{\omega}^{\mathrm{h}}} \tag{18}$$

where ρ_{h} is the density of the hydrate, kg/cm^3; θ_{l} and θ_{s} are the occupancy rates of large cavities and small cavities of hydrate, %; M_{m} and M_{w} are the molar mass of methane molecules and water molecules, respectively, g/mol; $\mu_{\omega}^{\mathrm{h}}$ is the molar volume of hydrate lattice, cm^3/mol.

(4) Saturation of hydrate samples

When preparing a hydrate sample, the porosity of the hydrate sample can be calculated according to the relevant parameters of the deformation amount and the prepared material when the deformation amount does not change:

$$\phi = \frac{V_{\phi}}{V_{\mathrm{samp}}} \times 100\% = \frac{V_{\mathrm{samp}} - V_{\mathrm{sand}}}{V_{\mathrm{samp}}} \times 100\% = \frac{\frac{\pi}{4}d_{\mathrm{samp}}^2 h_{\mathrm{samp}} - \frac{m_{\mathrm{sand}}}{\rho_{\mathrm{sand}}}}{\frac{\pi}{4}d_{\mathrm{samp}}^2 h_{\mathrm{samp}}} \times 100\% \tag{19}$$

where ϕ is the porosity of the hydrate sample, %; V_{ϕ} and V_{samp} are the volume of the pores and the sample, cm^3.

$$S_{\mathrm{h}} = \frac{V_{\mathrm{h}}}{V_{\phi}} \times 100\% = \frac{\frac{n_{\mathrm{dr}} - n_{\phi}^{\mathrm{h}} + n_{\phi}}{46} N_{\mathrm{h}} \mu_{\omega}^{\mathrm{h}}}{\frac{\pi}{4}d_{\mathrm{samp}}^2 h_{\mathrm{samp}} - \frac{m_{\mathrm{sand}}}{\rho_{\mathrm{sand}}}} \times 100\% \tag{20}$$

In the formula, S_{h} is the hydrate saturation, %; V_{h} and V_{ϕ} are the volumes of hydrates and pores, cm^3; n_{dr} is the amount of methane collected by the drainage method, mol; n_{ϕ} and n_{ϕ}^{h} are the amount of methane in the pores before and after hydrate formation, mol; and $\mu_{\omega}^{\mathrm{h}}$ is the lattice molar volume of the hydrate, cm^3/mol.

(5) Mechanical parameters of the sample

The deviatoric stress of the sample refers to the pressure difference between the axial pressure and the confining pressure, which can be calculated by the following formula:

$$\sigma_{\mathrm{d}} = \sigma_{\mathrm{a}} - \sigma_{\mathrm{c}} \tag{21}$$

where σ_{d}, σ_{a}, and σ_{c} are the deviatoric stress, axial pressure, and confining pressure of the sample, respectively, MPa.

The strain of the sample refers to the ratio of the deformation to the length of the sample after being loaded with axial compression, which can be calculated using the following formula:

$$\begin{cases} \Delta h = h_1 - h_0 \\ h = h_{\mathrm{samp}} - \Delta h \\ \varepsilon_{\mathrm{n}} = \frac{\Delta h}{h_{\mathrm{samp}}} \\ \varepsilon_{\mathrm{a}} = \frac{\Delta h}{h} \end{cases} \tag{22}$$

where Δh is the deformation of the sample, mm; h_1 is the displacement of the axial compression system, mm; h_0 is the initial displacement of the axial compression system, mm; h is the height of the sample, mm; ε_{n} is the nominal strain of the sample; and ε_{a} is the true strain of the sample.

According to the stress–strain curve under quasi-static loading conditions, some elastic parameters of the sample can be obtained:

$$\begin{cases} E = \left| \frac{\sigma_d}{\varepsilon_a} \right| \\ \nu = \left| \frac{\varepsilon_r}{\varepsilon_a} \right| \\ G = \frac{E}{2(1+\nu)} \\ K = \frac{E}{3(1-2\nu)} \end{cases} \quad (23)$$

where E is the Young's modulus, MPa; σ_d is the deviatoric stress, MPa; ε_a is the true axial strain of the specimen; ν is Poisson's ratio, obtained through the uniaxial compression test; ε_r is the radial strain of the sample, measured by strain gauges under uniaxial compression; G is the shear modulus, MPa; and K is the bulk modulus, MPa.

The cohesion and internal friction angle of the sample can be obtained according to the Mohr–Coulomb criterion:

$$\tau = c + \sigma \tan \theta \quad (24)$$

In the formula, τ is the shear strength, MPa; c is the cohesion force, MPa; σ is the normal stress, MPa; and θ is the internal friction angle.

2.2.3. Preparation Materials and Methods of Natural Gas Hydrate Samples

Due to the extremely low solubility of methane gas in water, it is difficult to form hydrate under artificial conditions. Therefore, in the preparation process, SDS (sodium dodecyl sulfate) solution with a concentration of 0.3 g/L was used instead of pure deionized water to increase the solubility of methane in water and promote the formation of methane hydrate [30].

(1) Sample preparation materials

Figure 2a–f are the tools and materials required for hydrate sample preparation.

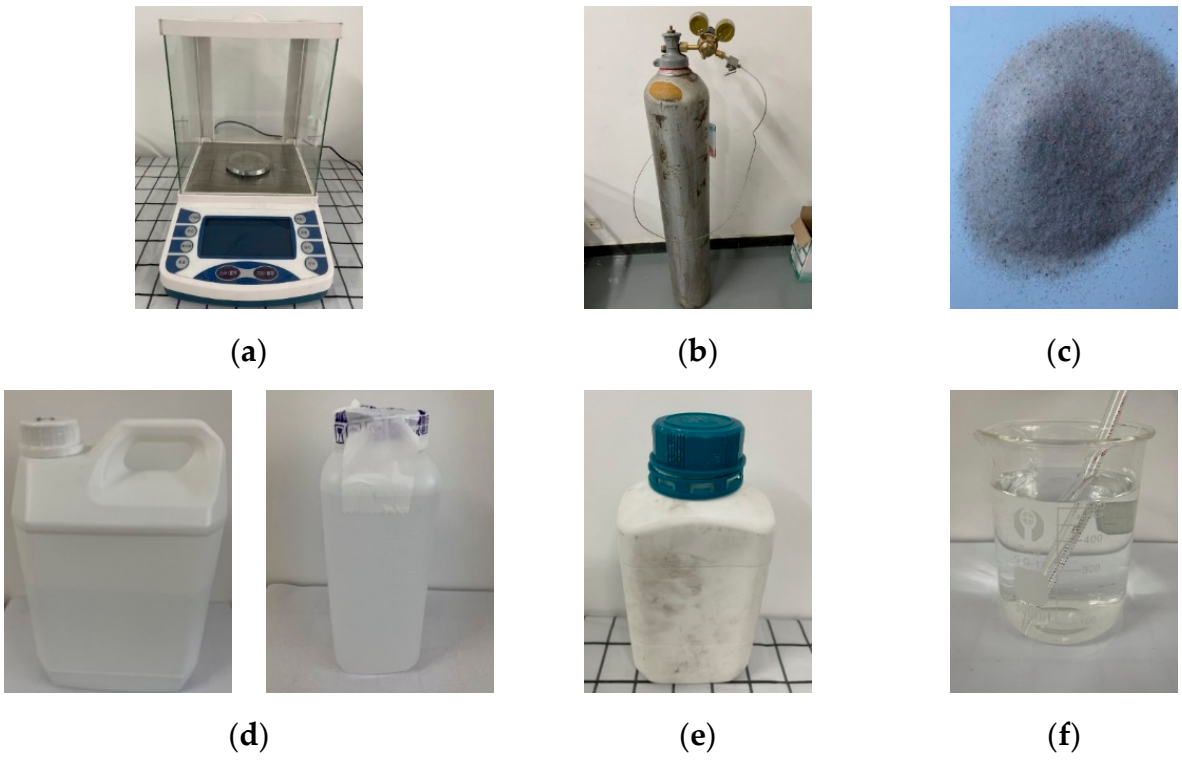

Figure 2. Tools and materials for samples preparation. (**a**) Electronic analytical balance. (**b**) Test gas. (**c**) Quartz sand. (**d**) Epoxy resin. (**e**) SDS. (**f**) Deionized water.

(2) Sample preparation method

The gas saturated method, i.e., excess gas and a fixed content of water, was used for the formation of hydrate samples in this study.

The consolidated diagenetic gas hydrate reservoir is supported by the formation skeleton; thus, the skeleton voids are filled by gas hydrate. We used the method of quartz sand epoxy resin cementation to make a supporting framework for the gas hydrate sample [31]. In this study, hydrate samples were prepared according to the following steps: standard sieves were used to screen quartz sands of different particle sizes for use, and a filter was laid at the bottom of the preparation kettle to prevent quartz sands from entering the gas channel; the quality of quartz sand, epoxy resin, and deionized water required were calculated, the quartz sand and epoxy resin were weighed with an electronic analytical balance, mixed thoroughly, placed in the preparation kettle, and the axial pressure control system was connected for sealing; the axial pressure control system began to pressurize the sample preparation device, with the pressure set to 15 MPa until the deformation did not change. The sample preparation device was then connected to the vacuum pump, and the inside of the preparation kettle was pumped to a vacuum state. The quartz sand was left for 24 h to ensure that it had fully cemented, and the temperature control system was initiated to adjust the temperature of the sample preparation device to the set temperature. The sample preparation device was then connected to the advection pump, and a certain amount of deionized water was injected into the preparation kettle, and a vacuum was used to suck the deionized water into the preparation kettle and distribute it evenly. The sample preparation device was then connected to the gas cylinder to maintain the pressure in the preparation tank at a higher level than the phase equilibrium pressure at the reaction temperature, and when the pressure in the preparation kettle was maintained above the phase equilibrium pressure for a long time and the pressure did not decrease after pressurization, the sample preparation ended.

(3) Hydrate triaxial mechanical test

In this study, the hydrate triaxial mechanical test was carried out according to the following steps: the temperature control system of the hydrate triaxial seepage test platform was initiated in order to reduce the temperature in the reactor to the test set temperature. The hydrate sample was put into a rubber sleeve with the same inner diameter as the sample at a thickness of 0.5 mm to avoid the influence of pressure fluid on the properties of the sample. The back-pressure plug was inserted into the rubber sleeve, connecting it with the top plug, rotating and sealing the reactor, and the axial pressure-loading system was initiated to apply an axial pressure greater than 0 to the sample. The confining pressure-loading system was used to load the back-pressure and confining pressure of the sample to the set value, and the axial compression loading system was used to apply axial pressure to the sample until it was broken. The confining pressure, back-pressure, and confining pressure were unloaded in sequence, and the sample was taken out and the test data were saved.

The pore pressure was controlled at 4 MPa and the temperature was controlled at 2 °C when performing the triaxial shear test under the net confining pressure.

2.3. Correction of P-Y Curves in Hydrate-Bearing Formation in Shallow Seabed

2.3.1. Calculation Method of the P-Y Curve in Shallow Submarine Formation

The p-y curve of the API standard was proposed by Matlock [32] and Reese [33] based on their experiments; it can be used to calculate the lateral foundation reaction force of the pipe side per unit area of sandy soil in shallow seabed formations:

$$\begin{cases} p(y) = \kappa p_{\mathrm{u}} \tanh\left(\frac{K_{\kappa} h}{\kappa p_{\mathrm{u}}} y\right) \\ \kappa = (3.0\text{–}0.8h/D_{\mathrm{c}}), \text{ Cyclic load} \\ \kappa = 0.9, \qquad\qquad \text{Static load} \end{cases} \tag{25}$$

where κ is the periodic or continuous static load factor; p_u is the lateral limit foundation reaction force of the foundation, kN/m; K_κ is the initial modulus coefficient of the reaction force of the sandy soil foundation, N/m^3; D_c is the pile diameter, m; h is the depth of the soil, m.

$$\begin{cases} p_{us} = (C_1 h + C_2 D_c)\gamma'_s h, & h < h_r; \\ p_{ud} = C_3 D_c \gamma'_s h, & h \geq h_r; \\ h_r = \frac{C_3 - C_2}{C_1} D_c \end{cases} \tag{26}$$

where γ'_s is the underwater gravity of the sandy soil, N/m^3; h_r is the depth of the boundary line between shallow sand and deep sand, m; C_1, C_2, and C_3 are the correlation coefficients of the internal friction angle.

$$\begin{cases} C_1 = \frac{k_0 \tan\theta \sin\beta}{\tan(\beta-\theta)\cos\alpha} + \frac{\tan^2\beta \tan\alpha}{\tan(\beta-\theta)} + k_0 \tan\beta(\tan\theta \sin\beta - \tan\alpha) \\ C_2 = \frac{\tan\beta}{\tan(\beta-\theta)} - \tan^2\left(\frac{\pi}{4} - \frac{\theta}{2}\right) \\ C_3 = \tan^2\left(\frac{\pi}{4} - \frac{\theta}{2}\right)(\tan^8\beta - 1) + k_0 \tan\theta \tan^4\beta \end{cases} \tag{27}$$

where θ is the internal friction angle of the soil, °; $k_0 = 0.4$, $\alpha = \frac{\theta}{2}$, and $\beta = \frac{\pi}{4} + \frac{\theta}{2}$.

The formula for calculating the error rate of the p-y curve is defined as follows:

$$\xi_e = \frac{p - p'}{p} \tag{28}$$

where ξ_e is the error rate; p is the foundation reaction force calculated by finite elements; and p' is the calculated foundation reaction force.

The error analysis of the calculation result error of each model was carried out using Equation (28).

2.3.2. Numerical Simulation of Pile–Soil Interaction

According to the previous test results, the finite element model of the shallow hydrate-bearing formation on the seabed was established using ABAQUS finite element analysis software. The soil boundary size of the calculation model was 500 mm × 500 mm × 1050 mm, and the soil was divided into upper, middle, and lower layers: the upper layer was a 50 mm sand layer; the middle layer was a hydrate formation with a thickness of 700 mm; and the lower layer was a 350 mm thick layer. For the sand cushion, the model pile was assembled in the middle of the soil model; the bottom of the pile was 350 mm from the bottom boundary of the soil model; and the horizontal loading surface was set at 20 mm from the top of the pile. A platform load of 200 tf was applied as a boundary condition, and the effective outer diameter of the pile leg was 1.66 m. Other relevant calculation parameters are shown in Tables 2–4.

Table 2. Parameters of model pipe piles.

Outer Diameter	Wall Thickness	Elastic Modulus	Poisson's Ratio	Density
1524 mm	54 mm	210 GPa	0.33	7580 kg/m^3

The Mohr–Coulomb constitutive model was used for the soil, and the elastic–plastic constitutive model was used for the model piles. The finite element calculation model adopted structured grid division, and the model pile and soil were divided into 5680 elements, and the pile–soil element type was selected as the C3D8R three-dimensional cubic shear integration element. The displacement in the x and y directions was constrained on the four sides of the soil model, and the bottom surface of the soil model was fixed at the same time.

Table 3. Environmental parameters.

Environmental Parameters			Value	Unit
	Water depth		28	m
	Height above sea level		15	m
	Wind speed		46	m/s
Wave parameters	Morrison Coefficient	Lateral drag coefficient	0.7	
		Tangential drag coefficient	0.0	
		Lateral inertia coefficient		
	Airy wave definition	Significant wave height		
		Significant wave period		
		Wavelength		
Ocean Current Parameters	Sea surface velocity		1.73	m/s
	Bottom Velocity		0.95	m/s
	Fluid density		1021	kg/m^3

Table 4. Mechanical parameters of hydrate samples with different saturations.

Saturation	Cohesion	Angle of Internal Friction	Young's Modulus
0%	4.52 kPa	29.92°	43 MPa
15%	90.40 kPa	33.39°	77 MPa
25%	273.29 kPa	35.90°	94 MPa
35%	295.01 kPa	38.01°	128 MPa

3. Results

3.1. Triaxial Shear Test of Hydrate Sediments with Different Saturations under Different Pore Pressure and Temperature Conditions

In order to improve the accuracy of the test, the analytical gas method was used to measure the saturation of the hydrate sample after the sample preparation had been completed; some sample data of the measured saturation that had deviated too much from the preset saturation were discarded. At the same time, in order to analyze the influence of saturation more intuitively, the measured saturation of the remaining hydrate samples was approximately treated according to the preset values of 5%, 15%, 25%, and 35%.

Figure 3 shows the phenomenon of triaxial shear test. Figure 4 shows the results of triaxial shear tests on hydrate samples with different saturations at different temperatures and pressures.

Figure 3. Triaxial compression test phenomenon of the sand hydrate sample.

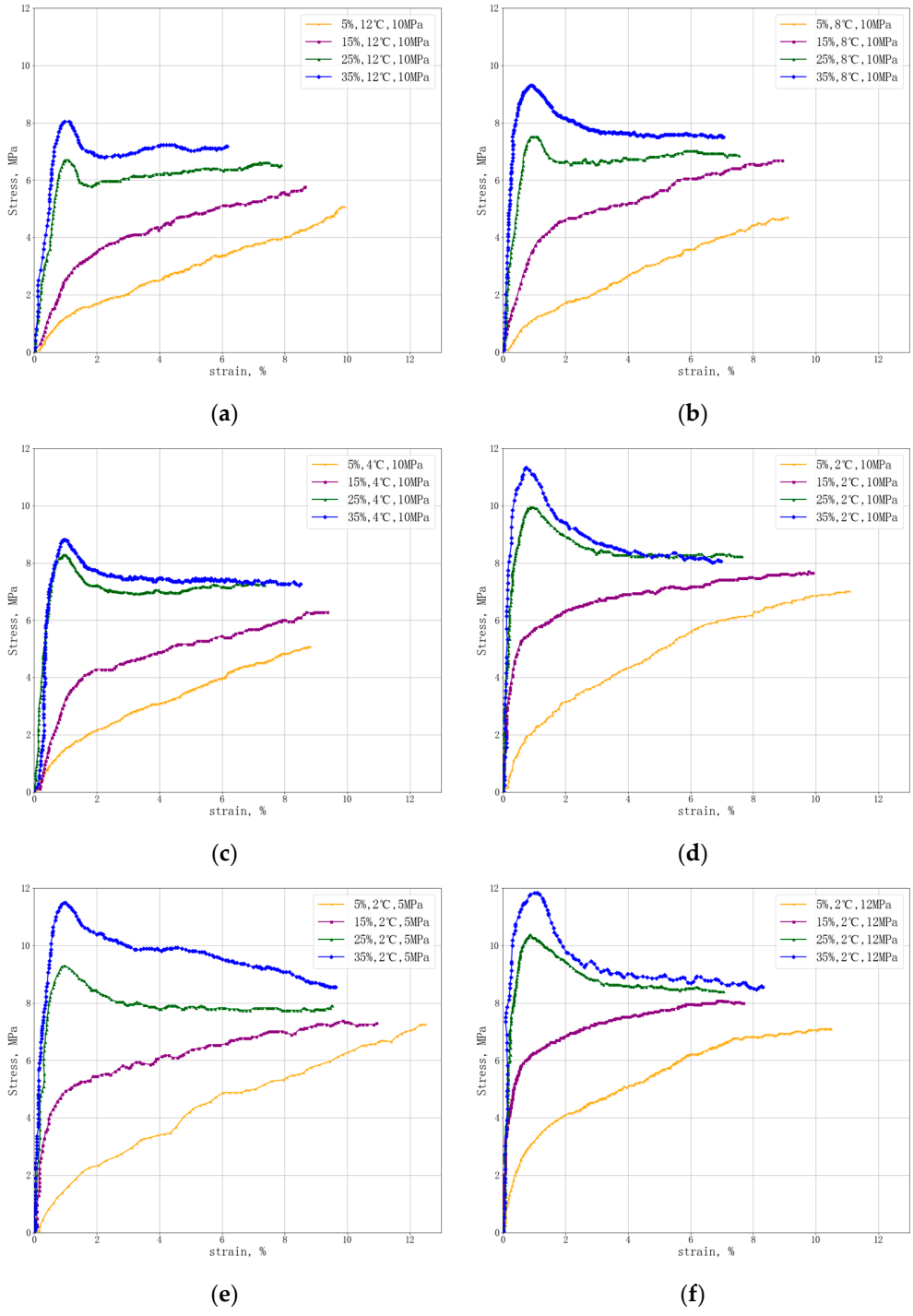

Figure 4. Figure 4. Stress–strain curves under different temperature and pressure conditions. (**a**) Stress–strain curves at 12 °C and 10 MPa. (**b**) Stress–strain curves at 8 °C and 10 MPa. (**c**) Stress–strain curves at 4 °C and 10 MPa. (**d**) Stress–strain curves at 2 °C and 10 MPa. (**e**) Stress–strain curves at 2 °C and 5 MPa. (**f**) Stress–strain curves at 2 °C and 12 MPa.

3.2. Triaxial Shear Test of Hydrate Sediments with Different Saturations under Different Net Confining Pressure Conditions

(1) Stress–strain curves of different hydrate saturations under different net confining pressures

Figure 5 shows the results of triaxial shear tests on hydrate samples with different saturation under different net confining pressures. The test temperature is 2 °C.

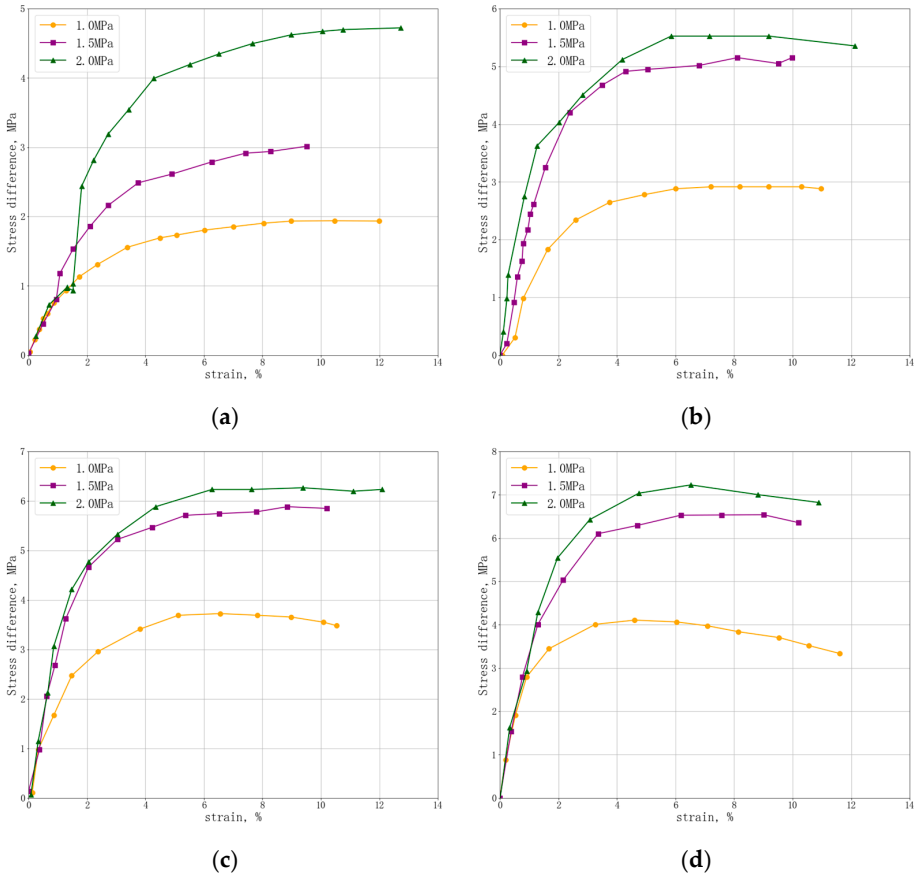

Figure 5. Stress–strain curves of different hydrate saturations under different net confining pressures. (**a**) Stress–strain curves at 0% saturation. (**b**) Stress–strain curves at 15% saturation. (**c**) Stress–strain curves of 25% saturation. (**d**) Stress–strain curves of 35% saturation.

(2) Angle of Internal Friction and Mohr's Circle

Figure 6 shows the Mohr circles calculated from triaxial shear test data.

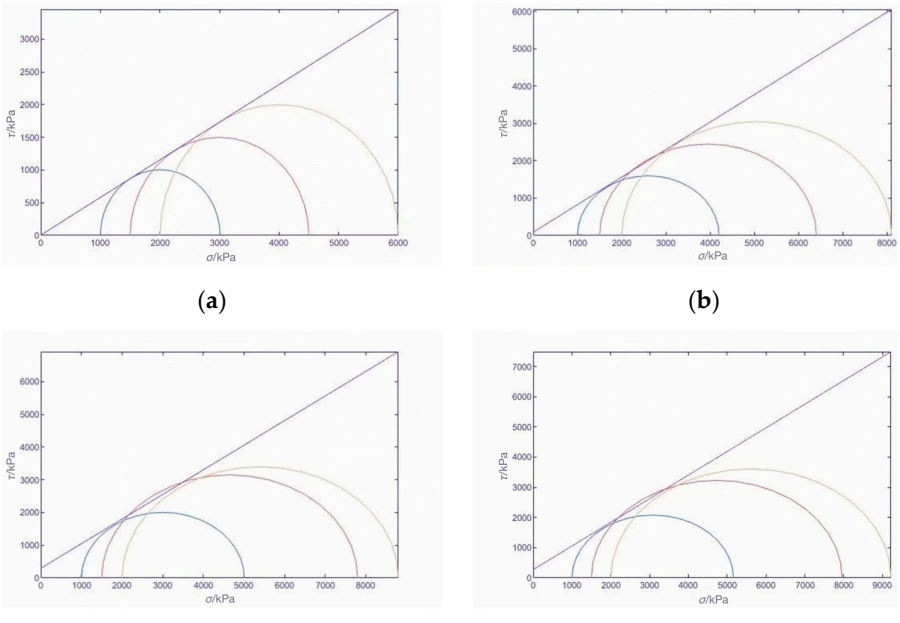

Figure 6. Mohr circles of hydrate deposits with different saturations. (**a**) Mohr circle at 0% saturation. (**b**) Mohr circle at 15% saturation. (**c**) Mohr circle at 25% saturation. (**d**) Mohr circle at 35% saturation.

According to the results of the triaxial shear test, the self-made MATLAB program drew the Mohr's circle and solved the internal friction angle and cohesion.

3.3. Numerical Simulation

3.3.1. Meshing of the Model

Figure 7 shows the pipe string and soil model.

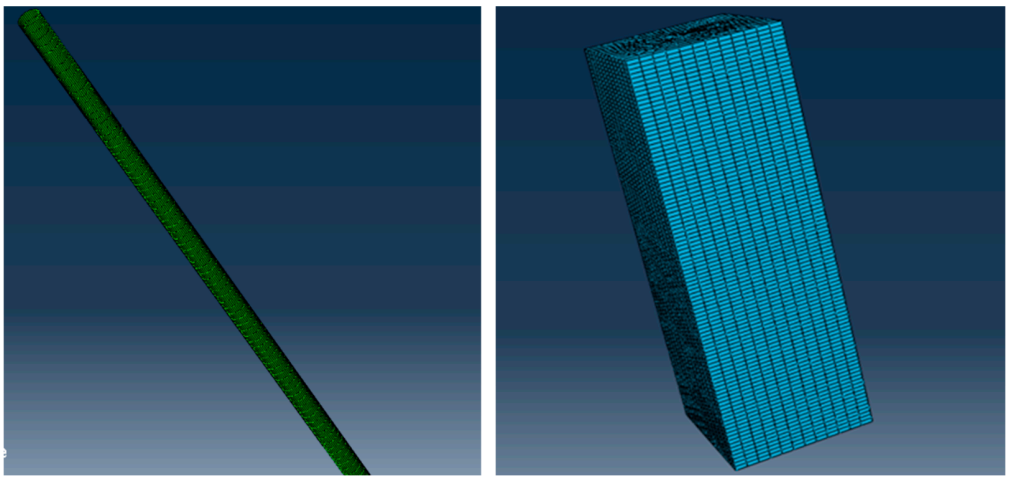

(**a**) (**b**)

Figure 7. Meshing of finite element models. (**a**) Pipe pile model. (**b**) Soil model.

3.3.2. Numerical Simulation Results

Figure 8 shows the p-y curves obtained by numerical simulation.

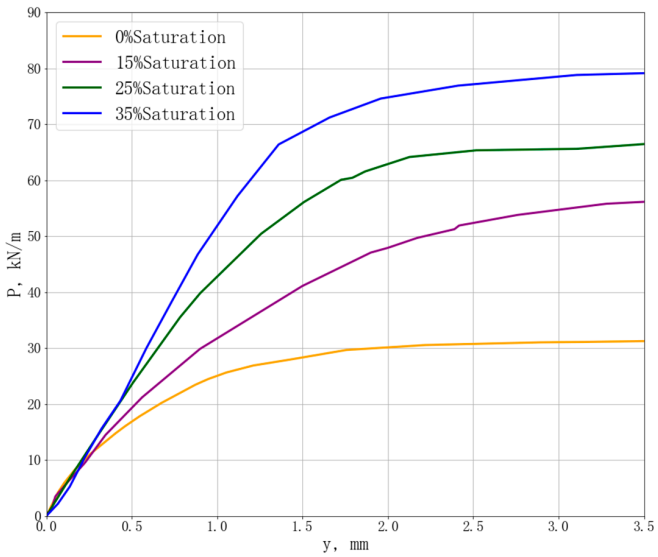

Figure 8. The p-y curves obtained by numerical simulation.

3.3.3. Correction of P-Y Curve

Through many trial calculations, it was found that the error rate of corrected curve 1 in Figures 9 and 10 is relatively small. In order to compare the ABAQUS calculation results with the API standard results more clearly, only corrected curve 2, which has a large error rate, is retained in Figures 9 and 10; other curves with larger error rates are not shown in the figure.

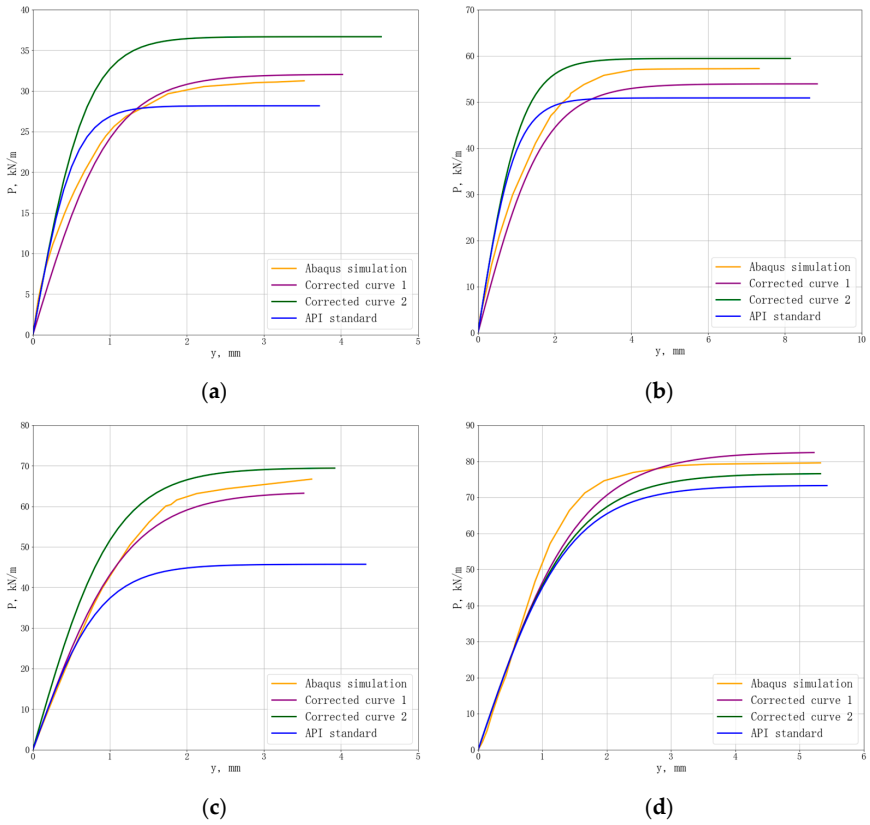

Figure 9. P-y curves of shallow seabed hydrate-bearing layers with different hydrate saturations. (**a**) P-y curve with 0% saturation. (**b**) P-y curve with 15% saturation. (**c**) P-y curve with 25% saturation. (**d**) P-y curve with 35% saturation.

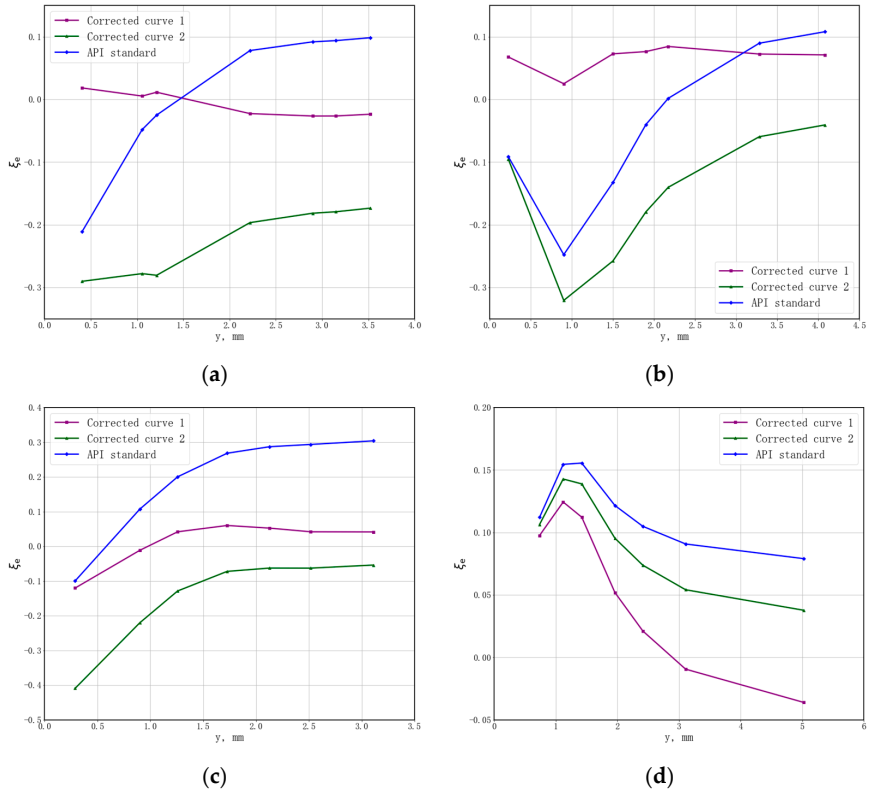

Figure 10. Error analysis of p-y curves. (**a**) Error analysis of 0% saturation. (**b**) Error analysis of 15% saturation. (**c**) Error analysis of 25% saturation. (**d**) Error analysis of 35% saturation.

The correction method of corrected curve 1 was corrected for α and K_κ using the following correction method:

$$\begin{cases} \alpha = \frac{2\theta}{3} \\ K_\kappa = \frac{0.768e^{0.1597\theta} + 0.549e^{0.0876\theta}}{3} \end{cases} \quad (29)$$

4. Discussion

4.1. Test Device and Sample Preparation Method

(1) The existing triaxial test device was improved so that it could perform the triaxial shear test under low-temperature conditions. The problem of inaccurate results caused by hydrate decomposition during the test was avoided.

(2) The new triaxial instrument could carry out the permeability measurement under the simulated real stress conditions of the formation. It could also be used to control sediment pore pressure during triaxial shearing. This function also controlled the sediment pore pressure during triaxial shearing.

4.2. Effects of Saturation, Pore Pressure, and Temperature on the Properties of Hydrate Deposits

The following conclusions can be drawn from Figure 4.

(1) When the hydrate saturation is high (25–35%), the hydrate in the pores plays a key role in supporting the sediment. The stress–strain curves have obvious peak intensities. After reaching the yield point, there is a clear strain-softening phenomenon, and the overall performance is characterized by strain softening.

(2) No other components (such as clay) in the hydrate layer sediment system were added during the preparation of hydrate deposits; therefore, the porosity of hydrate deposits was larger than that of real hydrate deposit samples. Additionally, when the hydrate saturation was low (5%~15%), the stress–strain curve had no obvious peak strength because the hydrate could not play a supporting role on the sample. After the inflection point, the growth trend of deviatoric stress slowed down but still increased slowly, characterized by overall strain hardening.

(3) The stress–strain curve of hydrate deposits increased rapidly in the small strain range, and there was a clear inflection point (at approximately 1% of the strain value).

(4) Under the same temperature and pore pressure conditions, the peak intensity of the sample clearly increased with the degree of saturation. Taking the conditions of 8 °C and 10 MPa as an example, the peak strength of the sample in the small strain range increased from 1.17 MPa (5%) to 9.18 MPa. The reason is that with the increase in saturation, the supporting effect of the hydrate on sediments becomes stronger.

(5) As the temperature decreased, the strength of hydrate sediments increased. Taking the conditions of 10 MPa and 35% saturation as an example, the peak strength of the sample dropped from 11.33 MPa to 8.04 MPa. As the temperature decreased, the cementation between hydrate particles in the sediments increased, and at the same time, the free water that did not form hydrates became stronger; thus, ice also played a key role in supporting the sediment.

(6) The increase in pore pressure also affected the strength of the sediments. Taking the conditions of 2 °C and 35% saturation as an example, the peak strength of the sample increased from 11.48 to 11.83 MPa. Pore pressure did not increase the strength of the sample as much as saturation and temperature.

(7) The saturation critical value of strain hardening and strain transformation of hydrate deposits was between 15% and 25%.

4.3. Effects of Hydrate Saturation and Net Confining Properties on the Strength of Hydrate Deposits

Due to the large error caused by the uneven distribution of hydrate in the sediment when the saturation was low, the 5% saturation data were discarded when analyzing the triaxial shear test under net confining pressure.

From Figures 5, 6, 9 and 10, the following conclusions can be summarized.

(1) With the increase in hydrate saturation, the maximum intensity of the stress–strain curve increased obviously, and the increase in the net confining pressure also led to the increase in the peak intensity. This is consistent with previous experimental results.

(2) As the hydrate saturation increased from 0% to 35%, the Young's modulus, cohesion, and internal friction angle increased from 43 MPa, 4.52 kPa, and 29.92° to 128 MPa, 295.01 kPa, and 38.01°, respectively.

(3) Using ABAQUS finite element analysis software, the p-y curves of shallow seabed formations containing hydrates with different saturations were calculated. Under the same displacement conditions, the maximum value of the foundation reaction force clearly increased with the increase in saturation.

(4) The error rate of the p-y curve of the API standard was large, and was thus not applicable to the hydrate layer.

(5) According to the ABAQUS simulation results, a large number of trial calculations were carried out. The calculation method of the error rate was defined, and a correction method for the p-y curve of the shallow seabed formation containing hydrates with different saturations was proposed, as shown in Equation (29).

5. Conclusions

In this study, the triaxial test device was improved on the basis of previous studies, so that it could meet the requirements of low-temperature triaxial shear tests, and could also simulate permeability measurements under real stress conditions. This helped to improve the precision of the test.

Unconsolidated undrained and consolidated undrained triaxial shear tests were carried out, and the results showed that the strength of hydrate deposits was enhanced by a decrease in temperature, an increase in pore pressure, and an increase in hydrate saturation. Saturation had the greatest impact on the strength of the sample, followed by temperature, with pressure having the least impact.

According to the results of the triaxial shear test, the internal friction angle and cohesion force were calculated using the self-made MATLAB program. Numerical simulations were carried out using ABAQUS, and it was found that the rate of error between the obtained p-y curve and the API standard curve was relatively large. Many trial calculations were carried out, and the p-y curve correction method suitable for shallow hydrate-bearing formations on the seabed was optimally obtained through error rate analysis.

Author Contributions: Conceptualization, H.D. and H.F.; methodology, H.D., Y.Y. (Yuguang Ye) and B.W.; software, R.J., B.W. and Z.Y.; validation, Y.L. and F.Z.; formal analysis, H.D. and B.W.; investigation, H.D. and B.W.; resources, H.F.; data curation, H.D., B.W. and Y.Y. (Yixiang Yang); writing—original draft preparation, H.D.; writing—review and editing, H.D.; visualization, H.D.; supervision, H.F.; project administration, H.F. and H.D.; funding acquisition, H.F. All authors have read and agreed to the published version of the manuscript.

Funding: This research received no external funding.

Institutional Review Board Statement: Not applicable.

Informed Consent Statement: Not applicable.

Data Availability Statement: Not applicable.

Conflicts of Interest: The authors declare no conflict of interest.

References

1. Zhu, Y.; Zhang, Y.; Wen, H.; Lu, Z.Q.; Jia, Y.Z.; Li, Y.H.; Li, Q.H.; Liu, C.L.; Wang, P.K.; Guo, X.W. Gas Hydrates in the Qilian Mountain Permafrost, Qinghai, Northwest China. *Acta Geol. Sin. Engl. Ed.* **2010**, *84*, 1–10. [CrossRef]
2. Sain, K.; Gupta, H. Gas hydrates in India: Potential and development. *Gondwana Res.* **2012**, *22*, 645–657. [CrossRef]
3. Diao, H.; Fan, H.; Leira, B.J.; Sangesland, S.; Ye, Y.; Liu, Y.; Zhou, F.; Wu, B.; Sevillano, L.C.; Yao, C. A Calculation Model for the Temperature Field of the Shallow Submarine Strata Considering the Heat of Hydration of Cement Slurry. In Proceedings of the Offshore Technology Conference, Huston, TX, USA, 2–5 May 2022. [CrossRef]
4. Lei, L.; Santamarina, J.C. Laboratory Strategies for Hydrate Formation in Fine-Grained Sediments. *J. Geophys. Res. Solid Earth* **2018**, *123*, 2583–2596. [CrossRef]
5. Li, Y.; Hu, G.; Wu, N.; Liu, C.; Chen, Q.; Li, C. Undrained shear strength evaluation for hydrate-bearing sediment overlying strata in the Shenhu area, northern South China Sea. *Acta Oceanol. Sin.* **2019**, *38*, 114–123. [CrossRef]
6. Wang, L.; Zhao, J.; Sun, X.; Wu, P.; Shen, S.; Liu, T.; Li, Y. Comprehensive review of geomechanical constitutive models of gas hydrate-bearing sediments. *J. Nat. Gas Sci. Eng.* **2021**, *88*, 103755. [CrossRef]
7. Wu, P.; Li, Y.; Sun, X.; Liu, W.; Song, Y. Mechanical Characteristics of Hydrate-Bearing Sediment: A Review. *Energy Fuels* **2021**, *35*, 1041–1057. [CrossRef]
8. Lee, S.; Holder, G.D. Methane hydrates potential as a future energy source. *Fuel Process. Technol.* **2001**, *71*, 181–186. [CrossRef]
9. Chong, Z.R.; Yang, S.H.B.; Babu, P.; Linga, P.; Li, X.-S. Review of natural gas hydrates as an energy resource: Prospects and challenges. *Appl. Energy* **2016**, *162*, 1633–1652. [CrossRef]
10. Li, Q.; Han, Y.; Liu, X.; Ansari, U.; Cheng, Y.; Yan, C. Hydrate as a by-product in CO_2 leakage during the long-term sub-seabed sequestration and its role in preventing further leakage. *Environ. Sci. Pollut. Res.* **2022**, *29*, 77737–77754. [CrossRef]
11. Li, Q.; Wang, F.; Wang, Y.; Zhou, C.; Chen, J.; Forson, K.; Miao, R.; Su, Y.; Zhang, J. Effect of reservoir characteristics and chemicals on filtration property of water-based drilling fluid in unconventional reservoir and mechanism disclosure. *Environ. Sci. Pollut. Res.* **2023**, *22*, 4447–4459. [CrossRef]
12. Li, Q.; Wu, J. Factors affecting the lower limit of the safe mud weight window for drilling operation in hydrate-bearing sediments in the Northern South China Sea. *Geomech. Geophys. Geo-Energy Geo-Resour.* **2022**, *8*, 82. [CrossRef]
13. Li, Y.; Song, Y.; Liu, W. Progress in Triaxial Compression Test of Natural Gas Hydrate. *Nat. Gas Explor. Dev.* **2010**, *33*, 51–55. (In Chinese)
14. Luo, T.; Song, Y.; Zhu, Y.; Liu, W.; Liu, Y.; Li, Y.; Wu, Z. Triaxial experiments on the mechanical properties of hydrate-bearing marine sediments of South China Sea. *Mar. Pet. Geol.* **2016**, *77*, 507–514. [CrossRef]
15. Miyazaki, K.; Tenma, N.; Yamaguchi, T. Relationship between creep property and loading-rate dependence of strength of artificial methane-hydrate-bearing Toyoura Sand under triaxial compression. *Energies* **2017**, *10*, 1466. [CrossRef]
16. Hyodo, M.; Wu, Y.; Nakashima, K.; Kajiyama, S.; Nakata, Y. Influence of Fines Content on the Mechanical Behavior of Methane Hydrate-Bearing Sediments. *J. Geophys. Res. Solid Earth* **2017**, *122*, 7511–7524. [CrossRef]
17. Li, Y.; Liu, C.; Liao, H.; Dong, L.; Bu, Q.; Liu, Z. Mechanical properties of mixed system of argillaceous silt sediment-gas hydrate. *Nat. Gas Ind.* **2020**, *40*, 159–168. (In Chinese)
18. Zhu, Y.; Wang, J.; Xu, Y.; Ying, Z. Comparative study on mechanical properties of methane and carbon dioxide hydrate sediments. *Unconv. Oil Gas* **2021**, *8*, 1–8. (In Chinese) [CrossRef]
19. Li, Y. Study on lateral dynamic response of pile foundation in liquefied soil. Harbin City, Heilongjiang Province, China: Institute of Engineering Mechanics. *China Seismol. Bur.* **2006**, *173–174*, 210. (In Chinese)
20. Qi, C. *Study on P-Y Curve of Pile-Soil Interaction during Liquefaction of Saturated Sand*; Tianjin University: Tianjin, China, 2008; pp. 89–102. (In Chinese)
21. Sloan, E.D. Fundamental principles and applications of natural gas hydrates. *Nature* **2003**, *426*, 353–359. [CrossRef]
22. Liu, C.; Meng, Q.; Li, C.; Sun, J.; He, X.; Yang, S.; Liang, J. Characteristics of gas hydrate and its deposit on the northern continental slope of the South China Sea. *Geosci. Front.* **2017**, *24*, 41–50. (In Chinese) [CrossRef]
23. Ji, P. Experimental study on different pore saturation of coal body containing gas hydrate. *Coal Mine Saf.* **2019**, *50*, 27–31. (In Chinese) [CrossRef]
24. Du, Y.; Guo, T. Prediction of hydrate formation for systems containing methanol. *Chem. Eng. Sci.* **1990**, *45*, 893–900. [CrossRef]
25. Parrish, W.R.; Prausnitz, J.M. Dissociation Pressures of Gas Hydrates Formed by Gas Mixtures. *Ind. Eng. Chem. Process Des. Dev.* **1972**, *11*, 26–35. [CrossRef]
26. Wang, Z. *Study on Flow Regime Transformation Mechanism of Annular Multiphase Flow with Natural Gas Hydrate Phase Change*; China University of Petroleum (East China): Qingdao, China, 2009; pp. 13–14. (In Chinese)
27. Voronov, V.P.; Gorodetskii, E.E.; Podnek, V.E.; Grigoriev, B. Properties of equilibrium carbon dioxide hydrate in porous medium. *Chem. Phys.* **2016**, *476*, 61–68. [CrossRef]
28. Li, W. *Experimental Study on Physical Parameters of Natural Gas Hydrate Sediment*; Southwest Petroleum University: Chengdu, China, 2019; p. 18, (In Chinese). [CrossRef]
29. Dong, M. *Experimental Study on Basic Physical Properties of Hydrate Sediment*; Southwest Petroleum University: Chengdu, China, 2017; p. 25. (In Chinese)
30. Roosta, H.; Khosharay, S.; Varaminian, F. Experimental study of methane hydrate formation kinetics with or without additives and modeling based on chemical affinity. *Energy Convers. Manag.* **2013**, *76*, 499–505. [CrossRef]

31. Sothcott, J.; Ellis, M.H.; Best, A.I.; Frerichs, N.R.; Minshull, T.A.; Sinha, M.C. Laboratory observations of morphology, velocity, attenuation and resistivity of methane-gas-hydrate-bearing rocks. *Soc. Explor. Geophys.* **2007**, 1530–1534. [CrossRef]
32. Matlock, H. Correlation for Design of Laterally Loaded Piles in Soft Clay. In Proceedings of the Offshore Technology Conference, Houston, TX, USA, 21–23 April 1970. [CrossRef]
33. Reese, L.C.; Cox, W.R.; Koop, F.D. Analysis of Laterally Loaded Piles in Sand. In Proceedings of the Offshore Technology Conference, Houston, TX, USA, 5–7 May 1974. [CrossRef]